Resolving seasonal rainfall changes in the Middle East during the last interglacial period

Ian J. Orland[a,1,2], Feng He[b], Miryam Bar-Matthews[c], Guangshan Chen[a], Avner Ayalon[c], and John E. Kutzbach[b]

[a]Department of Geoscience, University of Wisconsin–Madison, Madison, WI 53706; [b]Center for Climatic Research, Nelson Institute for Environmental Studies, University of Wisconsin–Madison, Madison, WI 53706; and [c]Department of Geochemistry, Geological Survey of Israel, Jerusalem 9692100, Israel

Edited by Katherine H. Freeman, Pennsylvania State University, University Park, PA, and approved October 22, 2019 (received for review February 21, 2019)

Paleorainfall proxy records from the Middle East have revealed remarkable patterns of variability since the penultimate glacial period (140 ka), but the seasonality of this signal has been unresolvable. Here, seasonal-resolution oxygen isotope data from Soreq Cave speleothems suggest that summer monsoon rainfall periodically reaches as far north as Israel—well removed from the modern monsoon—at times (~125, 105 ka) that overlap with evidence for some of the earliest modern human migrations out of Africa. These seasonal proxy data are corroborated by seasonal-resolution model output of the amount and oxygen-isotope ratio of rainfall from an isotope-enabled climate model. In contrast to the modern regional climate where rainfall is delivered predominantly in winter months along westerly storm tracks, the model suggests that during extreme peaks of summer insolation—as occurs during the last interglacial (e.g., 125, 105 ka)—regional rainfall increases due to both wetter winters and the incursion of summer monsoons. This interpretation brings clarity to regional paleoproxy records and provides important environmental context along one potential pathway of early modern human migration.

paleoclimate | seasonal-resolution | oxygen isotopes | data-model comparison

The oxygen isotope ($\delta^{18}O$) record from Soreq Cave (Israel; Fig. 1) carbonate formations (speleothems) is a remarkable paleoclimate archive from a region of critical importance to understanding early migration of modern humans (1, 2), the development of civilization (3, 4), and Late Quaternary hydroclimate dynamics (5–7). The composite $\delta^{18}O$ record from Soreq speleothems (7, 8) spans the last 185 ka and has low-frequency variations of multiple per mil that align with precession forcing of northern hemisphere insolation (Fig. 2). The timing and magnitude of this variability has been hypothesized to reflect, in part, precessionally forced monsoon flooding from North Africa that stratifies into a low-$\delta^{18}O$ freshwater lens atop the eastern Mediterranean (EM) Sea, inducing anoxic conditions and organic-rich sedimentation ("sapropels") at the EM seafloor when northern hemisphere summer insolation is high (9–12). The resulting decline of $\delta^{18}O$ values in EM surface water could then be transmitted to the cave site, where modern rainfall is sourced predominantly from the Mediterranean (5, 13).

Another potential contribution to the precession-paced pattern of $\delta^{18}O$ variability observed in Soreq is a northward expansion of summer monsoon circulation derived from the tropics during periods of high northern hemisphere insolation. At Soreq, the effect of Rayleigh fractionation (14) on distally sourced monsoon rainfall would result in low-$\delta^{18}O$ summer rainfall that would decrease the annually averaged $\delta^{18}O$ of rainfall above the cave. The connection between precession-paced insolation changes and summer monsoon dynamics (15) is well-established in records of speleothem $\delta^{18}O$ from elsewhere in Asia (16, 17). Confoundingly, however, this pattern of $\delta^{18}O$ variability is also observed in speleothems from parts of Asia beyond the limits of the modern summer monsoon including Kesang Cave (Fig. 1) in northwestern China (18) and Soreq (6), which currently has a dry summer and receives most of its rainfall from westerly winter storm tracks. Some paleorainfall proxy records from the Middle East independently suggest that, indeed, the northern limit of summer monsoon rainfall delivery expands during precessional peaks in northern hemisphere (NH) insolation (e.g., 176, 125, 105, 85 ka) beyond its modern boundary to reach the Arabian Peninsula (19, 20) and the Levant (21, 22). In notable contrast, a modeling study that compares the regional climate dynamics in the EM between periods of maximum (125 ka) and minimum (115 ka) seasonal insolation gradient emphasizes that winter westerly storm tracks may deliver increased moisture to these regions when winter insolation is minimized (and summer insolation is maximized) (23). This emphasis on winter rainfall is invoked to explain increased moisture in the Levant at 125 ka (peak summer insolation) in a separate set of paleoclimate records (24, 25). Clearly, disentangling seasonal components of Middle Eastern paleoclimate records is critical for resolving the dynamics of monsoon variability as well as the interpretive differences in regional paleoclimate records. Together, these advances would elucidate a vital dimension of the environmental context for modern human migrations out of Africa.

Here, we take a 2-pronged approach to evaluating the seasonal paleoclimate of the Middle East. First, rainfall simulations in an isotope-enabled climate model are used to examine the feasible geographic limits of summer monsoon rainfall and its

Significance

The Middle East was a gateway for early human migration out of Africa, and it is likely that the region's climate played an important role in this anthropogenic transition. This study is motivated by conflicting interpretations of rainfall seasonality from regional paleoenvironmental records. Specifically, we address whether summer monsoon rainfall may have expanded northward into the Middle East in the past. Today, the region has dry summers and relatively wet winters; the northern limit of the modern monsoon is far to the south. Here, we combine climate modeling with seasonal-resolution geochemical analysis of cave carbonates from Israel and find evidence for summer monsoon rainfall during recurrent intervals of the last interglacial period, which overlaps with archeological indicators of human migration.

Author contributions: I.J.O. and F.H. designed research; I.J.O., F.H., and G.C. performed research; I.J.O., F.H., M.B.-M., G.C., A.A., and J.E.K. analyzed data; and I.J.O., F.H., M.B.-M., G.C., A.A., and J.E.K. wrote the paper.

The authors declare no competing interest.

This article is a PNAS Direct Submission.

Data deposition: All climate model data generated in this study are available at Open Science Framework (DOI: 10.17605/OSF.IO/FHQD5) and are available upon request.

[1]To whom correspondence may be addressed. Email: orland@wisc.edu.

[2]Present address: Wisconsin Geological and Natural History Survey, University of Wisconsin–Madison, Madison, WI 53705.

This article contains supporting information online at https://www.pnas.org/lookup/suppl/doi:10.1073/pnas.1903139116/-/DCSupplemental.

First published November 25, 2019.

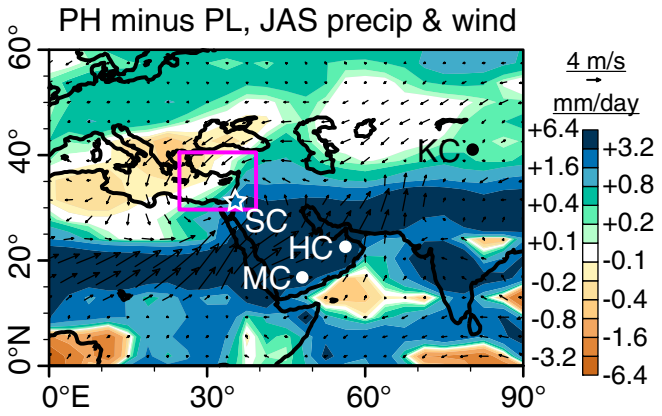

Fig. 1. Model results showing changes in summer (JAS) precipitation amount (millimeters per day; note the logarithmic color scale) at 125 ka (PH, maximum summer insolation) relative to 115 ka (PL, minimum summer insolation) and associated changes in the speed (meters per second) and direction of surface winds. Superimposed are the locations of Soreq Cave in Israel (SC, star), the geographic region examined in this and earlier global climate simulations (23) (pink rectangle), and the locations of paleoclimate records referenced in the text (Kesang Cave, KC; Hoti Cave, HC; Mukalla Cave, MC). The locations of paleoclimate records from the Dead Sea and the Negev Desert overlap with the star symbol.

isotopic signature. Given the well-established link between NH summer monsoon strength and summer insolation, modeling targeted the precession-forced summer insolation maximum at 125 ka—the highest summer insolation peak during the last 185 ka of the Soreq speleothem record. Two comparative model runs were completed at sequential extremes of insolation seasonality (Fig. 2)—that is, Precession-High NH seasonality (PH; 125 ka) and Precession-Low NH seasonality (PL; 115 ka). The modeled amount and $\delta^{18}O$ of monthly rainfall was then extracted for the Levant region.

Next, we used an ion microprobe (or secondary ion mass spectrometer, "SIMS") to test whether seasonal $\delta^{18}O$ signals recorded in Soreq speleothems at PH and PL are coherent with the model results for the Levant. The ion microprobe enables high-resolution (10-μm-diameter spots) in situ $\delta^{18}O$ sampling of speleothem calcite, in contrast to conventional drill-sampling techniques that are limited to millimeter-scale resolution. Combined with imaging of fluorescent growth banding in the Soreq speleothems, multiple ion microprobe analyses (n = 2 to 9) were placed across individual annual growth bands to measure and compare patterns of seasonal $\delta^{18}O$ variability through time. Given the subannual resolution of the ion microprobe $\delta^{18}O$ data, they must be treated in populations—much like weather observations—in order to interpret persistent changes in seasonal climate. This analytical approach was first developed in speleothem samples from Soreq Cave (refs. 26 and 27 and *SI Appendix*) and builds on an extended cave-monitoring program that has characterized Soreq hydrology (28) and demonstrated how seasonal climate signals are transmitted to the geochemistry of a modern Soreq speleothem (29). The current study leverages this extensive prior work at Soreq Cave to probe a crucial frontier in paleoclimate research: seasonal-resolution proxy-model comparison.

Results

First, rainfall $\delta^{18}O$ is simulated by forcing an atmospheric model that incorporates $\delta^{18}O$ of rain and water vapor (the isotope-enabled Community Atmosphere Model, isoCAM3) with boundary conditions derived from coupled global climate simulations of PH and PL in the Community Climate System Model (CCSM3) (see *Materials and Methods*). Rainfall amount and rainfall $\delta^{18}O$ output are averaged from the EM region using the same geographic boundaries as the prior modeling study (23) (Fig. 1) and binned into monthly intervals (Fig. 3).

Next, we compare the range of $\delta^{18}O$ variability ($\Delta^{18}O$) observed within growth bands of 2 speleothems from Soreq Cave at time slices during precession-paced maxima (~125, 105 ka) and minimum (~115 ka) seasonal insolation gradients (Fig. 4). Earlier work describes the hydrology of the cave and demonstrates that $\Delta^{18}O$ in Soreq speleothems is a robust proxy of seasonal hydroclimate (26, 28, 29). In brief, seasonal variation of $\delta^{18}O$ is observed in modern Soreq rainwaters, dripwaters, and speleothem growth bands with lowest $\delta^{18}O$ values during the winter wet season. The geochemistry and drip rates of modern Soreq dripwaters suggest that cave water is sourced from 2 reservoirs: a "baseline" reservoir with multidecadal residence time supplies dripwater to the cave year-round, while a second reservoir delivers the more intense rains of the winter wet season (low-$\delta^{18}O$) to the cave along more direct flowpaths (refs. 26 and 28–30 and *SI Appendix*). Hence, as previously corroborated in a modern Soreq speleothem, increased rainfall during a winter wet season correlates with lower $\delta^{18}O$ values of winter dripwaters relative to the baseline reservoir and results in a predictable increase in $\Delta^{18}O$ (28, 29). If, at 125 ka, low-$\delta^{18}O$ monsoon rainfall were added to the summertime Levant hydroclimate, we hypothesize that $\Delta^{18}O$ within the growth bands of Soreq speleothems would have been smaller than at 115 ka because the additional summer rainfall would reduce the seasonal variability of dripwater $\delta^{18}O$ by decreasing the relative $\delta^{18}O$ of the baseline dripwater reservoir.

Model results indicate that monthly rainfall totals and rainfall $\delta^{18}O$ (Fig. 3 and *SI Appendix*) in the Levant are dramatically different during PH and PL, during both summer and winter seasons. At PL boundary conditions, the CCSM3–isoCAM3 climate model pairing generates spatial and monthly rainfall patterns in the Levant that resemble the modern climate; the majority of annual rainfall occurs during a winter wet season when $\delta^{18}O_{rain}$ is lowest. For PH boundary conditions, model output indicates increased winter rainfall but also significant northward expansion of the African and Asian summer monsoon belt (Fig. 1), such that there is significant rainfall during summer months (defined here as July-August-September [JAS], when PH rainfall $\delta^{18}O$ is distinctly lower than PL) in the Levant. Northward monsoon penetration in the Middle East is enhanced by westward expansion of the summertime "Persian Trough" low-pressure system (31); this latitudinal extension of monsoon rainfall is independently observed in other models (32–34). In our model results for the region shown in Fig. 1, there is a >4× increase in average JAS precipitation rate (0.15 to 0.67 mm/d; Fig. 3) in PH vs. PL, and the new summer rainfall has a low $\delta^{18}O$ value similar to that of the modeled (and modern) winter precipitation. Notably, the modeled difference between precipitation and evaporation over land in the Levant is similar in both simulations and exhibits little seasonal change (*SI Appendix*). Hence, we predict that rainfall over the cave during PH has similarly low $\delta^{18}O_{rain}$ values during the wettest winter and summer months, which would result in lower intraannual $\delta^{18}O$ variability ($\Delta^{18}O$) in Soreq Cave speleothems.

Soreq Cave speleothem samples "SO-15" and "3-35" were previously dated with the U-Th geochronometer and analyzed for $\delta^{18}O$ by conventional drilling methods (6, 8). For this study, imaging by confocal laser fluorescent microscopy (CLFM) revealed fluorescent banding in both samples akin to that observed in Soreq samples that grew during and after the last deglaciation (27). Earlier work finds repeated couplets of fluorescent ("bright") and nonfluorescent ("dark") bands in Soreq Cave speleothems to be annual markers with fluorescent domains interpreted as wet seasons when organic matter in the overlying soil is flushed into the cave (29). Soreq speleothem sample SO-15 grew during both PH and PL and thus was ideal for comparing seasonal $\delta^{18}O$ gradients during both time

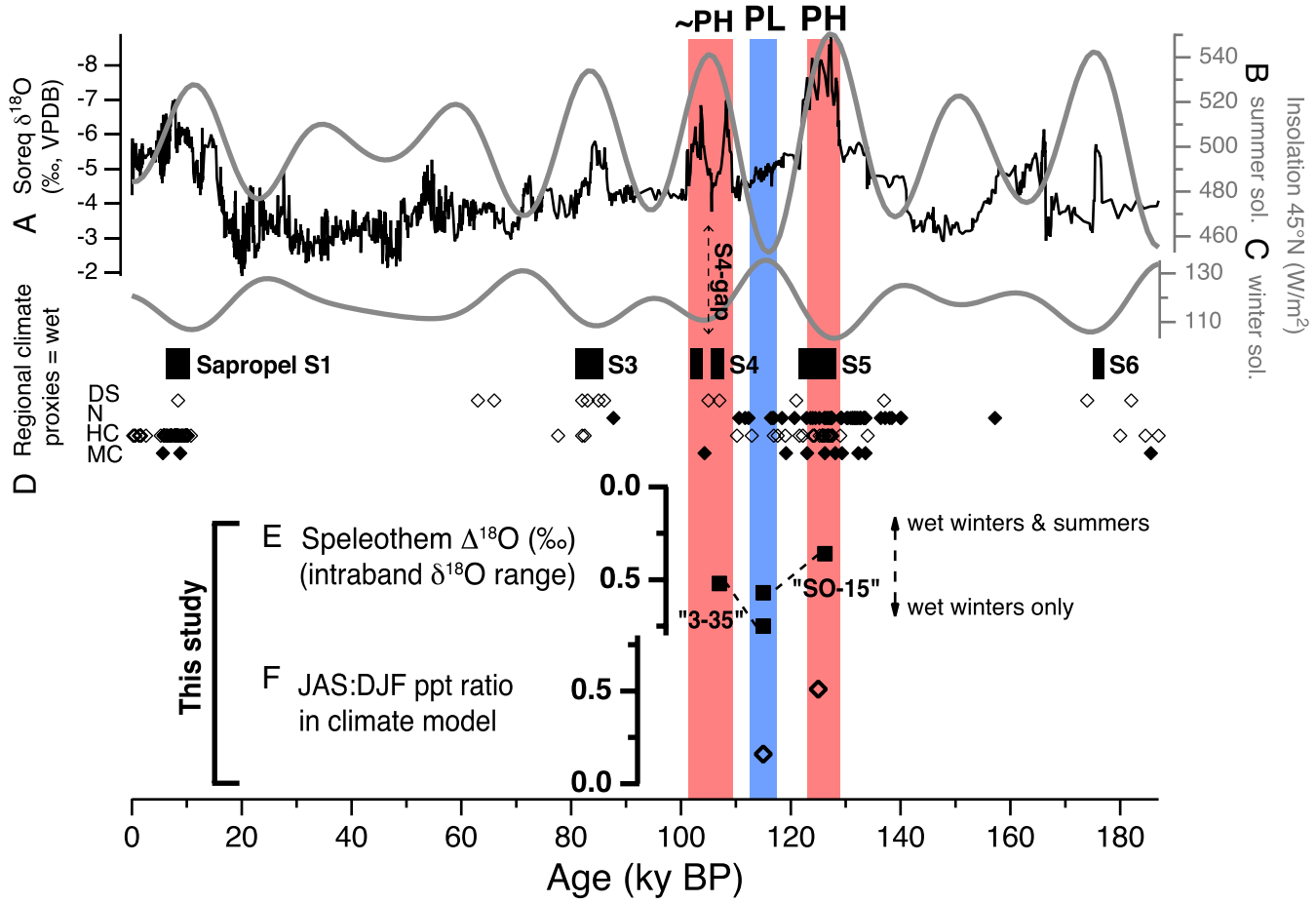

Fig. 2. Multiplot of the composite Soreq Cave $\delta^{18}O$ record since 185 ka (7, 8) (note the inverted axis) (*A*), 45°N summer solstice (*B*), and winter solstice insolation (*C*), with bars highlighting PH, PL, and the PH analog, ~PH. The timing of EM sapropel formation (*D*) in response to increased African monsoon rainfall (11, 12) is shown along with a prominent interruption of sapropel event 4 (S4-gap). Also presented are regional hydroclimate proxy indications of increased moisture near the Dead Sea (DS) (21), Negev Desert (N) (25), and at 2 caves on the Arabian Peninsula (HC and MC after Fig. 1) (19, 20). From this study (*E*), the mean seasonal $\delta^{18}O$ range ($\Delta^{18}O$; inverted axis) measured in 2 Soreq speleothems ("SO-15" and "3-35") is plotted for PH, PL, and ~PH time periods. The modeled ratio of summer (JAS) to winter (DJF) precipitation amount is illustrated (*F*) for the EM study region outlined in Fig. 1.

periods. Sample 3-35 grew during PL and the preceding precession-paced NH insolation maximum ("~PH"; ~110 to 101 ka), which includes a brief interruption of sapropel event 4 (S4-gap; Fig. 2) that coincides with a return of the Soreq $\delta^{18}O$ record to PL-like values (~108 to 105 ka; ref. 12). We make the analogous comparison in sample 3-35 of ~PH to combined observations from PL and the S4-gap interval in order to assess whether patterns of seasonal variability corroborate those observed in sample SO-15. Including both samples, a total of 601 SIMS analyses of $\delta^{18}O$ in 10-μm spots were completed (Dataset S1). This total includes multiple spots (between 2 and 9 spots each) in ~50 individual bands in each sample.

In order to compare $\delta^{18}O$ variability within individual growth bands, we normalized the distance between SIMS analyses in the dark portion of sequential growth bands. Fig. 4*A* schematically illustrates the placement, classification, and normalization of multiple SIMS analyses within a single fluorescent growth band. Fig. 4*B* shows the $\delta^{18}O$ variability across 2 representative bands in sample SO-15 superimposed on the normalized distance scale and demonstrates how $\Delta^{18}O$ is calculated as the difference between the $\delta^{18}O$ of the bright fluorescent domain ("b"; winter wet season dripwater) and the dark domain ("d"; summer "baseline" dripwater) at the end of the prior band. All normalized intraband $\delta^{18}O$ data are plotted for each sample in *SI Appendix*, Fig. S1. A binned bootstrap randomization of the dataset from each sample (*Materials and Methods* and *SI Appendix*, Fig. S1) shows that the observed intraband $\delta^{18}O$ variability lies outside a randomized distribution with 95% confidence.

We highlight 3 key observations from the results. First, the patterns of intraband $\delta^{18}O$ variability are not random (*SI Appendix*, Fig. S1*B*). Second, the $\delta^{18}O$ value of bright domains is consistently the lowest measured within a band, regardless of time period (*SI Appendix*, Fig. S1*A*). Third, the magnitude of intraband $\delta^{18}O$ change ($\Delta^{18}O$) differs between PH and PL (Figs. 2*E* and 4*C*). Mean $\Delta^{18}O$ in sample SO-15 is 0.36 during PH and increases to 0.57 during PL. In sample 3-35, mean $\Delta^{18}O$ is 0.52 during ~PH but is 0.73 for PL and S4-gap. The statistical significance of these changes in $\Delta^{18}O$ was then assessed as in prior work at Soreq (27).

The results of 2 statistical tests support the hypothesis that $\Delta^{18}O$ in Soreq speleothems during PH conditions would be different, and lower, with the addition of summer monsoon rainfall. First, a Kolmogorov–Smirnov test indicates, for both speleothems, that populations of $\Delta^{18}O$ values measured during PH vs. PL conditions are from statistically distinct ($P < 0.05$), normal distributions. Second, a 2-sample *t* test finds, again for both samples, that mean $\Delta^{18}O$ is smaller during PH than PL at the 95% confidence level (Fig. 4*C*). Further details are available in *SI Appendix*.

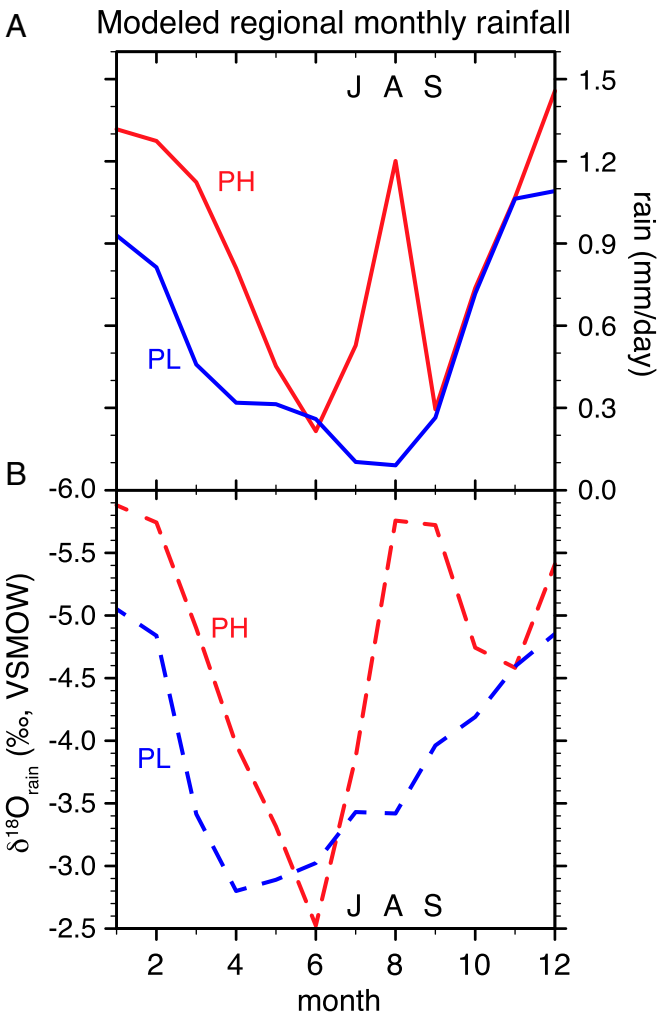

Fig. 3. Modeled monthly rainfall totals (*A*) and $\delta^{18}O$ of rainfall (*B*) in PH (red) vs. PL (blue) simulations. Summer months are labeled JAS. Note inverted $\delta^{18}O$ axis.

Discussion

To contextualize the observed decrease of seasonal $\delta^{18}O$ variability in Soreq speleothems at PH conditions, there are a number of climatic mechanisms with indirect and direct effects at Soreq Cave to consider. Here, we examine the expected impact of these mechanisms on the $\delta^{18}O$ of rainfall above Soreq Cave. First, an indirect effect on the source of Soreq rainfall: during PH, enhanced summer monsoon rainfall over northeast Africa increases Nile River outflow, causing EM surface water to freshen and weaken vertical mixing, which prompts sapropel formation in the EM (9, 10). The down-stream effect of this sequence on Soreq Cave—independent of changes in local climate—is to lower the $\delta^{18}O$ value of rainfall sourced from the EM. If the only precipitation at Soreq during PH was winter rainfall sourced from the EM, then the $\delta^{18}O$ of annually averaged rainfall at Soreq would be expected to decrease but the observed seasonal bias would not be imparted.

Likewise, the direct effects of predicted surface temperature and rainfall amount during PH vs. PL cannot explain the observed difference in $\Delta^{18}O$. Rainfall-monitoring and modern speleothem analysis at Soreq Cave shows that during the present-day winter-dominant rainfall regime, surface temperature positively correlates with rainfall $\delta^{18}O$ and rainfall amount negatively correlates with rainfall $\delta^{18}O$ (28, 29). Thus, neither the predicted warmer summers nor wetter winters of PH (23, 25) are, by themselves, consistent with smaller $\Delta^{18}O$ values.

Similarly, model results from this study combined with observations from the modern cave indicate that evaporation of surface and/or groundwater is unlikely to impart the observed $\Delta^{18}O$ signal. The modeled balance of evaporation and precipitation in the PH simulation is similar to PL (i.e., a modern analog) with little seasonal change. Since year-round sampling of modern dripwaters in Soreq Cave does not find an isotopic signature of evaporation (28), it is assumed that infiltration of rainwater at PH would also lack an isotopic signature of evaporation (*SI Appendix*). In sum, an additional climatic effect is needed to explain the decrease in $\Delta^{18}O$ values observed at PH.

The direct effect suggested by our rainfall isotope-enabled modeling is the northward expansion during PH of low-$\delta^{18}O$, summer monsoon rainfall that is most extensive along a corridor through the Middle East from the Indian Ocean to the shores of the EM (Fig. 1). Relative to PL, when rainfall above Soreq Cave is delivered almost entirely by winter westerlies, the northward expansion of summer monsoon rainfall would act to both reduce annual rainfall $\delta^{18}O$ and decrease seasonal $\delta^{18}O$ variability recorded in speleothems. This mechanism offers a self-consistent explanation for both the seasonal-resolution speleothem geochemistry results of this study and model realizations of PH and PL. The combination of our geochemical and model results provides a clear resolution to the intriguing ambiguity (35) of when and where monsoonal rainfall might impact the Mediterranean region.

Regional paleoclimate proxies have confounded this question with conflicting interpretations. One group of paleoclimate records dismiss the possibility of monsoonal expansion to the Mediterranean, but they either do not sample during PH or an equivalent insolation optimum (36, 37) or evaluate the Mediterranean basin as a whole (35)—our model suggests that the monsoon impact is confined to the EM. In contrast, another suite of regional paleoclimate proxies from pollen (38, 39), travertine (21), speleothem (19, 25, 40), relict lake deposits (41), leaf waxes (42), and Dead Sea sediment (22) records indicate increased moisture during PH along the Middle Eastern corridor between Indian Ocean and EM. Taken alone, however, these records cannot unambiguously assess the source or seasonality of additional moisture. To this end, earlier climate models provide support for the general northward expansion of monsoon rainfall during PH, but not far enough north to replicate either the increased summer moisture (43, 44) or decreased rainfall $\delta^{18}O$ values (45) interpreted from proxies. A more recent modeling study (23), however, does show increased winter and summer rainfall in the Middle East at PH and emphasizes the importance of verifying this result with proxy observations.

Our interpretation of increased winter rainfall and an expanded range of the African–Asian summer monsoon to as far north as the Levant along a Middle Eastern corridor at ~125 and ~105 ka brings clarity to a rich collection of climate proxy records in the region. Furthermore, this conclusion infers a remarkably dynamic latitudinal range of the summer monsoon that is sensitive to the periodic variation of NH insolation. One implication that warrants further investigation of this type is on the duration, periodic timing, and geographic limits of habitable pathways for human migration out of Africa (46–48). Although it is still debated whether (49) or not (42) early human migrations out of Africa coincide with humid periods, we note that the age of the earliest human remains recently found in the Levant (2) may align with an analog of PH at ~176 ka (Fig. 2*A* and refs. 7 and 50). Our conclusion supports the hypothesis that drastic changes in regional moisture availability that could enable such migration transpired on a recurring basis across the Pleistocene.

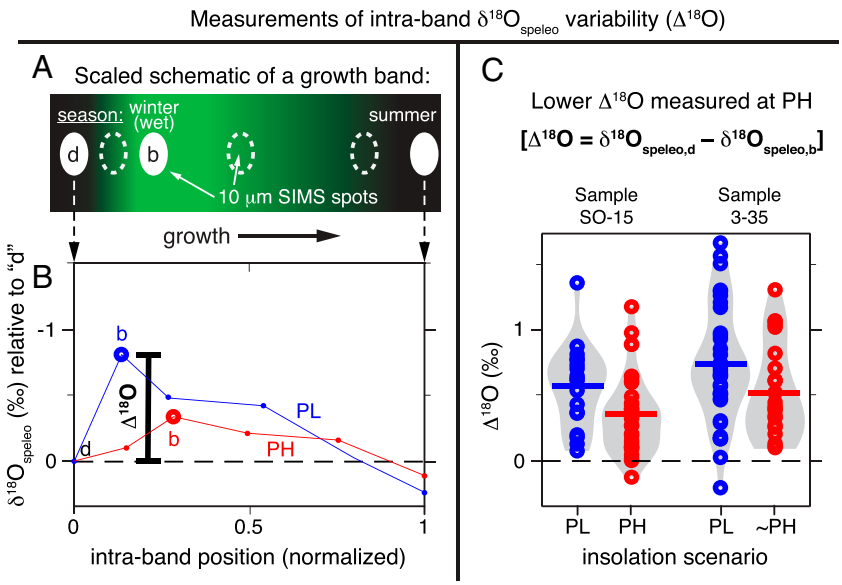

Fig. 4. Summary of intraband speleothem $\delta^{18}O$ variability. (*A*) Scaled schematic of SIMS spots in dark ("d"; summer "baseline" dripwater) and bright ("b"; winter wet season dripwater) fluorescent portions of a speleothem growth band, with 3 to 10 spots in each band (including the dark spot "d" at the end of the preceding band). (*B*) Intraband $\delta^{18}O$ variability relative to "d" in 2 representative growth bands from Soreq speleothem "SO-15". The horizontal axis is scaled from the end of the preceding band (=0) to the end of the current band (=1). Values of $\delta^{18}O$ measured in each band (small circles) are connected by red (PH) or blue (PL) lines. Large circles mark the SIMS spot "b" in the bright fluorescent portion of each band and are the lowest $\delta^{18}O$ value measured in each band (note the inverted vertical axis). Calculation of $\Delta^{18}O$ is illustrated for a single band and is the difference in the $\delta^{18}O$ of the "b" and "d" spots. (*C*) For both Soreq speleothems analyzed in this study, measured $\Delta^{18}O$ values are plotted for both PL (blue circles) and PH (red) periods. To help visualize differences between $\Delta^{18}O$ in each insolation scenario, mean values are marked with a horizontal line and the probability density (with Gaussian kernel) is illustrated with a gray envelope.

Materials and Methods

Speleothem Analysis. In preparation for ion microprobe analysis, subsamples of Soreq Cave speleothems 3-35 and SO-15 (*SI Appendix*, Fig. S2) were ground flat for imaging using a water-lubricated, fixed-diamond lapping pad. In order to confirm the existence of fluorescent banding, samples were imaged by CLFM at the University of Wisconsin Optical Imaging Core on a Nikon A1Rs inverted-geometry microscope. A 488-nm-excitation laser induced fluorescence that was imaged using 4× and 10× objective lenses to generate 1,024 × 1,024 pixel, tagged image file-formatted files (pixel dimension, 0.94 μm). Further description of this imaging method can be found in earlier studies (26, 51).

Speleothem subsamples were then cut along an analytical transect, parallel to the direction of crystal growth. These transects were then subdivided into 15-mm-long pieces that were cast 2-at-a-time (tip-to-tail), along with 3 grains of the University of Wisconsin (UW) calcite standard UWC-3 (12.49‰ Vienna Standard Mean Ocean Water [VSMOW]; ref. 52), into 1-inch round epoxy mounts. After casting, each mount was ground flat with a rotating 9-μm-grit fixed-diamond lapping pad and then polished by a sequence of 6-, 3-, and 1-μm-grit polycrystalline diamond suspensions on low-nap, rotating polishing pads. A final polish was achieved with a colloidal alumina suspension (0.05 μm) that enhanced the quality of subsequent CLFM imaging. This second round of CLFM imaging was used to navigate and identify targets for $\delta^{18}O$ analysis by ion microprobe. Following CLFM imaging, the sample was coated with a thin layer of gold to a thickness of 60 nm in order to facilitate charge-compensation during ion-microprobe analysis.

Ion-microprobe analysis of speleothem calcite $\delta^{18}O$ was completed on the large-radius multicollector CAMECA IMS 1280 secondary ion mass spectrometer in the WiscSIMS laboratory at UW–Madison. Analysis of both samples was completed over the course of five 12-h days divided into 3 sessions between October 2017 and March 2018. For each session, a ∼1.3-nA primary beam of $^{133}Cs^+$ ions with 20 keV impact energy was focused to a diameter of 9 μm on the sample surface. The primary beam sputtered oval-shaped spots—9 × 12 μm in dimension—into the sample surface to a depth of ∼1 μm. Ionized components of the sputtered material ("secondary ions") were accelerated into the double-focusing mass spectrometer, which was tuned to simultaneously collect $^{16}O^-$, $^{18}O^-$, and the molecular ion species $^{16}O^1H^-$ on 3 Faraday cups. The resulting count rate for $^{16}O^-$ during calcite analyses was ∼2.5 × 10^9 counts per second.

Ion-microprobe analyses are standardized using a bracketing technique whereby each group of 12 to 16 sample analyses is bracketed by 2 sets of typically 4 analyses of the calcite standard UWC-3. The external precision of a block of sample analyses is reported as the 2 SD of the 8 bracketing standard analyses. In order to place the raw $\delta^{18}O$ values of a bracket of sample analyses onto the VSMOW scale, we use the mass bias calculated from the average raw $\delta^{18}O$ value of the bracketing standards. For ease of comparison, VSMOW values are converted to the Vienna Peedee Belemnite scale (VPDB, ref. 53). Results of each ion-microprobe analysis, including raw and standardized values, are reported in a comprehensive data table available online (Dataset S1). Postprocessing and quality control of ion-microprobe data are explained in detail in *SI Appendix*. All speleothem data generated in this study are entirely contained within *SI Appendix* and Dataset S1.

The normalized, intraband $\delta^{18}O$ variability for each speleothem sample was plotted and binned in MATLAB (54) using the qualitative fluorescence classifications and the spot positions as measured in the open-source geographic information system software, QGIS (*SI Appendix* and refs. 55 and 56). The bootstrap randomization of the intraband $\delta^{18}O$ data were also completed in MATLAB. For this, the $\delta^{18}O$ data for each band were randomly redistributed, then normalized and binned as done with the original data. This randomization and binning was repeated 100 times and the resulting distribution of binned averages was used to define the 95% confidence interval for randomly distributed $\delta^{18}O$ values that is illustrated in *SI Appendix*, Fig. S1.

Isotope-Enabled Climate Modeling. We performed the global rainfall isotope simulations for PH (125 ka) and PL (115 ka) with isotope-enabled isoCAM3 (57). The isotope-enabled isoCAM3 incorporates stable water isotopes into the National Center for Atmospheric Research (NCAR) atmospheric general circulation model CAM3 in T31 resolution with fractionation associated with surface evaporation and cloud processes (58). We ran the isotope-enabled isoCAM3 atmosphere model with boundary conditions from equilibrium coupled climate simulations from low-resolution NCAR CCSM3 (59) forced by orbital configurations and greenhouse gases at 125 and 115 ka, respectively. We used the same preindustrial surface ocean $\delta^{18}O$ values in both PH and PL isoCAM3 simulations to isolate the fractionation associated with atmospheric processes. Figs. 1–3 show precipitation and wind output from the isoCAM3 model. Ocean water $\delta^{18}O$ in this model does not respond to runoff or meteoric water. The climate model datasets generated and used for this

study are available at the publicly accessible Open Science Framework (DOI: 10.17605/OSF.IO/FHQD5).

ACKNOWLEDGMENTS. We acknowledge B. Hess for sample preparation; J. Valley and the WiscSIMS laboratory; J. Fournelle, B. Schneider, and the UW–Madison Wilcox scanning electron microscope laboratory; R. Tan, L. Rodenkirch, and the UW–Madison Optical Imaging Core; and the University of Michigan Stable Isotope Laboratory. We also acknowledge high-performance computing support from Yellowstone (ark:/85065/d7wd3xhc) and Cheyenne (DOI: 10.5065/D6RX99HX) provided by the Computational and Information Systems Laboratory at the National Center for Atmospheric Research, sponsored by the NSF. This research used resources of the Oak Ridge Leadership Computing Facility at the Oak Ridge National Laboratory, supported by the Office of Science of the US Department of Energy. Computing was supported under Department of Energy Contract DE-AC05-00OR22725. WiscSIMS is supported by NSF Grants EAR-1355590 and EAR-1658823 and UW–Madison. This research is supported by NSF Grants 1603065 (to I.J.O., F.H., and G.C.), 1231155 (to I.J.O.), and 1702407 (to I.J.O.), and by the Smithsonian's Human Origins Program (to F.H. and J.E.K.). Sample mounts analyzed in this study are curated at the UW–Madison Geology Museum. We acknowledge with thanks the comments of the editor and anonymous reviewers that led to substantial revision and clarification of the original manuscript.

1. C. B. Stringer, R. Grün, H. P. Schwarcz, P. Goldberg, ESR dates for the hominid burial site of Es Skhul in Israel. *Nature* **338**, 756–758 (1989).
2. I. Hershkovitz *et al*., The earliest modern humans outside Africa. *Science* **359**, 456–459 (2018).
3. N. Roberts, *The Holocene: An Environmental History* (John Wiley & Sons, 2014).
4. D. J. Kennett, J. P. Kennett, Early state formation in southern Mesopotamia: Sea levels, shorelines, and climate change. *J. Island Coast. Archaeol.* **1**, 67–99 (2006).
5. M. Bar-Matthews, A. Ayalon, A. Kaufman, Timing and hydrological conditions of Sapropel events in the Eastern Mediterranean, as evident from speleothems, Soreq cave, Israel. *Chem. Geol.* **169**, 145–156 (2000).
6. M. Bar-Matthews, A. Ayalon, M. Gilmour, A. Matthews, C. J. Hawkesworth, Sea–land oxygen isotopic relationships from planktonic foraminifera and speleothems in the Eastern Mediterranean region and their implication for paleorainfall during interglacial intervals. *Geochim. Cosmochim. Acta* **67**, 3181–3199 (2003).
7. M. Bar-Matthews, J. Keinan, A. Ayalon, Hydro-climate research of the late Quaternary of the Eastern Mediterranean-Levant region based on speleothems research–A review. *Quat. Sci. Rev.* **221**, 105872 (2019).
8. K. M. Grant *et al*., Rapid coupling between ice volume and polar temperature over the past 150,000 years. *Nature* **491**, 744–747 (2012).
9. M. Rossignol-Strick, W. Nesteroff, P. Olive, C. Vergnaud-Grazzini, After the deluge: Mediterranean stagnation and sapropel formation. *Nature* **295**, 105–110 (1982).
10. E. J. Rohling, G. Marino, K. M. Grant, Mediterranean climate and oceanography, and the periodic development of anoxic events (sapropels). *Earth Sci. Rev.* **143**, 62–97 (2015).
11. M. Rossignol-Strick, M. Paterne, A synthetic pollen record of the eastern Mediterranean sapropels of the last 1 Ma: Implications for the time-scale and formation of sapropels. *Mar. Geol.* **153**, 221–237 (1999).
12. K. M. Grant *et al*., The timing of Mediterranean sapropel deposition relative to insolation, sea-level and African monsoon changes. *Quat. Sci. Rev.* **140**, 125–141 (2016).
13. Y. Enzel *et al*., The climatic and physiographic controls of the eastern Mediterranean over the late Pleistocene climates in the southern Levant and its neighboring deserts. *Global Planet. Change* **60**, 165–192 (2008).
14. W. Dansgaard, Stable isotopes in precipitation. *Tellus* **16**, 436–468 (1964).
15. J. E. Kutzbach, Monsoon climate of the Early Holocene: Climate experiment with the Earth's orbital parameters for 9000 years ago. *Science* **214**, 59–61 (1981).
16. Y. J. Wang *et al*., A high-resolution absolute-dated late Pleistocene Monsoon record from Hulu Cave, China. *Science* **294**, 2345–2348 (2001).
17. H. Cheng, A. Sinha, X. Wang, F. W. Cruz, R. L. Edwards, The Global Paleomonsoon as seen through speleothem records from Asia and the Americas. *Clim. Dyn.* **39**, 1045–1062 (2012).
18. H. Cheng *et al*., The climatic cyclicity in semiarid-arid central Asia over the past 500,000 years. *Geophys. Res. Lett.* **39**, L01705 (2012).
19. D. Fleitmann *et al*., Holocene and Pleistocene pluvial periods in Yemen, southern Arabia. *Quat. Sci. Rev.* **30**, 783–787 (2011).
20. D. Fleitmann, S. J. Burns, U. Neff, A. Mangini, Changing moisture sources over the last 330,000 years in Northern Oman from fluid-inclusion evidence in speleothems. *Quat. Res.* **60**, 223–232 (2003).
21. N. Waldmann, A. Torfstein, M. Stein, Northward intrusions of low- and mid-latitude storms across the Saharo-Arabian belt during past interglacials. *Geology* **38**, 567–570 (2010).
22. A. Torfstein *et al*., Dead Sea drawdown and monsoonal impacts in the Levant during the last interglacial. *Earth Planet. Sci. Lett.* **412**, 235–244 (2015).
23. J. E. Kutzbach, G. Chen, H. Cheng, R. L. Edwards, Z. Liu, Potential role of winter rainfall in explaining increased moisture in the Mediterranean and Middle East during periods of maximum orbitally-forced insolation seasonality. *Clim. Dyn.* **42**, 1079–1095 (2014).
24. S. McGarry *et al*., Constraints on hydrological and paleotemperature variations in the Eastern Mediterranean region in the last 140ka given by the δD values of speleothem fluid inclusions. *Quat. Sci. Rev.* **23**, 919–934 (2004).
25. A. Vaks, M. Bar-Matthews, A. Matthews, A. Ayalon, A. Frumkin, Middle-Late Quaternary paleoclimate of northern margins of the Saharan-Arabian Desert: Reconstruction from speleothems of Negev Desert, Israel. *Quat. Sci. Rev.* **29**, 2647–2662 (2010).
26. I. J. Orland *et al*., Climate deterioration in the Eastern Mediterranean as revealed by ion microprobe analysis of a speleothem that grew from 2.2 to 0.9 ka in Soreq Cave, Israel. *Quat. Res.* **71**, 27–35 (2009).
27. I. J. Orland *et al*., Seasonal resolution of Eastern Mediterranean climate change since 34ka from a Soreq Cave speleothem. *Geochim. Cosmochim. Acta* **89**, 240–255 (2012).
28. A. Ayalon, M. Bar-Matthews, E. Sass, Rainfall-recharge relationships within a karstic terrain in the Eastern Mediterranean semi-arid region, Israel: $\delta^{18}O$ and δD characteristics. *J. Hydrol.* **207**, 18–31 (1998).
29. I. J. Orland *et al*., Seasonal climate signals (1990–2008) in a modern Soreq Cave stalagmite as revealed by high-resolution geochemical analysis. *Chem. Geol.* **363**, 322–333 (2014).
30. A. Kaufman, M. Bar-Matthews, A. Ayalon, I. Carmi, The vadose flow above Soreq Cave, Israel: A tritium study of the cave waters. *J. Hydrol.* **273**, 155–163 (2003).
31. E. Tyrlis, J. Lelieveld, B. Steil, The summer circulation over the eastern Mediterranean and the Middle East: Influence of the South Asian monsoon. *Clim. Dyn.* **40**, 1103–1123 (2013).
32. M. Mohtadi, M. Prange, S. Steinke, Palaeoclimatic insights into forcing and response of monsoon rainfall. *Nature* **533**, 191–199 (2016).
33. D. S. Battisti, Q. Ding, G. H. Roe, Coherent pan-Asian climatic and isotopic response to orbital forcing of tropical insolation. *J. Geophys. Res.* **119**, 11,997–12,020 (2014).
34. J. H. C. Bosmans *et al*., Precession and obliquity forcing of the freshwater budget over the Mediterranean. *Quat. Sci. Rev.* **123**, 16–30 (2015).
35. P. C. Tzedakis, Seven ambiguities in the Mediterranean palaeoenvironmental narrative. *Quat. Sci. Rev.* **26**, 2042–2066 (2007).
36. H. W. Arz, F. Lamy, J. Pätzold, P. J. Müller, M. Prins, Mediterranean moisture source for an early-Holocene humid period in the northern Red Sea. *Science* **300**, 118–121 (2003).
37. D. Langgut, A. Almogi-Labin, M. Bar-Matthews, M. Weinstein-Evron, Vegetation and climate changes in the South Eastern Mediterranean during the Last Glacial-Interglacial cycle (86 ka): New marine pollen record. *Quat. Sci. Rev.* **30**, 3960–3972 (2011).
38. R. Cheddadi, M. Rossignol-Strick, Eastern Mediterranean Quaternary paleoclimates from pollen and isotope records of marine cores in the Nile Cone Area. *Paleoceanography* **10**, 291–300 (1995).
39. A. Develle *et al*., A 250 ka sedimentary record from a small karstic lake in the Northern Levant Paleoclimatic implications. *Palaeogeogr. Palaeoclimatol. Palaeoecol.* **305**, 10–27 (2011).
40. S. Mehterian *et al*., Speleothem records of glacial/interglacial climate from Iran forewarn of future Water Availability in the interior of the Middle East. *Quat. Sci. Rev.* **164**, 187–198 (2017).
41. T. M. Rosenberg *et al*., Humid periods in southern Arabia: Windows of opportunity for modern human dispersal. *Geology* **39**, 1115–1118 (2011).
42. J. E. Tierney, P. B. deMenocal, P. D. Zander, A climatic context for the out-of-Africa migration. *Geology* **45**, 1023–1026 (2017).
43. W. L. Prell, J. E. Kutzbach, Monsoon variability over the past 150,000 years. *J. Geophys. Res.* **92**, 8411 (1987).
44. N. de Noblet, P. Braconnot, S. Joussaume, V. Masson, Sensitivity of simulated Asian and African summer monsoons to orbitally induced variations in insolation 126, 115 and 6 kBP. *Clim. Dyn.* **12**, 589–603 (1996).
45. M. Herold, G. Lohmann, Eemian tropical and subtropical African moisture transport: An isotope modelling study. *Clim. Dyn.* **33**, 1075–1088 (2009).
46. A. Frumkin, O. Bar-Yosef, H. P. Schwarcz, Possible paleohydrologic and paleoclimatic effects on hominin migration and occupation of the Levantine Middle Paleolithic. *J. Hum. Evol.* **60**, 437–451 (2011).
47. A. Vaks *et al*., Desert speleothems reveal climatic window for African exodus of early modern humans. *Geology* **35**, 831–834 (2007).
48. N. Boivin, D. Q. Fuller, R. Dennell, R. Allaby, M. D. Petraglia, Human dispersal across diverse environments of Asia during the Upper Pleistocene. *Quat. Int.* **300**, 32–47 (2013).
49. N. A. Drake, R. M. Blench, S. J. Armitage, C. S. Bristow, K. H. White, Ancient watercourses and biogeography of the Sahara explain the peopling of the desert. *Proc. Natl. Acad. Sci. U.S.A.* **108**, 458–462 (2011).
50. J. E. Kutzbach, X. Liu, Z. Liu, G. Chen, Simulation of the evolutionary response of global summer monsoons to orbital forcing over the past 280,000 years. *Clim. Dyn.* **30**, 567–579 (2008).
51. I. J. Orland *et al*., Direct measurements of deglacial monsoon strength in a Chinese stalagmite. *Geology* **43**, 555–558 (2015).
52. R. Kozdon, T. Ushikubo, N. T. Kita, M. Spicuzza, J. W. Valley, Intratest oxygen isotope variability in the planktonic foraminifer N. pachyderma: Real vs. apparent vital effects by ion microprobe. *Chem. Geol.* **258**, 327–337 (2009).
53. T. B. Coplen, C. Kendall, J. Hopple, Comparison of stable isotope reference samples. *Nature* **302**, 236–238 (1983).
54. MATLAB, Version R2018a (The Mathworks, Inc., Natick, MA, 2018).
55. QGIS Development Team, QGIS Geographic Information System, Version 2.18 (Open Source Geospatial Foundation Project, 2018).
56. B. Linzmeier, K. Kitajima, A. Denny, J. Cammack, Making maps on a micrometer scale. *Eos* **99**, 24–28 (2018).
57. Z. Liu *et al*., Chinese cave records and the East Asia Summer Monsoon. *Quat. Sci. Rev.* **83**, 115–128 (2014).
58. D. Noone, C. Sturm, "Comprehensive dynamical models of global and regional water isotope distributions" in *Isoscapes: Understanding Movement, Pattern, and Process on Earth through Isotope Mapping*, J. B. West, G. J. Bowen, T. E. Dawson, K. P. Tu, Eds. (Springer Netherlands, Dordrecht, The Netherlands, 2010), pp. 195–219.
59. S. G. Yeager, C. A. Shields, W. G. Large, J. J. Hack, The low-resolution CCSM3. *J. Clim.* **19**, 2545–2566 (2006).